Geo-Resilience 2023 Conference, Cardiff, Wales
D.G. Toll & M.G. Winter (Eds)
British Geotechnical Association, London. 2024
https://doi.org/10.53243/Geo-Resilience-2023-1-11

Modelling Translational Landslides in Strain-softening Soils

Wangcheng ZHANG

[1]Durham University, Durham, United Kingdom
Corresponding author: Wangcheng Zhang (wangcheng.zhang@durham.ac.uk)

Abstract

Landslides are a major geohazard worldwide, posing significant threats to infrastructure and human lives. Natural sensitive clays undergo strain softening during shearing, characterised by distinct peak and residual shear strengths. Translational landslides in strain-softening soils are usually enormous in size. Attention has been paid separately to slope stability analyses and post-failure dynamic analysis in previous studies. This study establishes an original numerical package for time-efficient modelling of the entire landslide evolution covering the pre-failure shear band propagation, slab failure and post-failure dynamics by using two methods, including an arbitrary Lagrangian-Eulerian Finite Element method and a depth-integrated finite volume method. The strain softening and rate dependency are considered for natural soils. The post-failure behaviours in the sliding layer, such as retrogression upslope and frontally confined mechanisms downslope, are simulated. Because of the easy implementation and efficiency, the proposed numerical methods for modelling of translational landslides seems promising for practical applications. The pros and cons of the two methods are discussed with three cases studies. Using the large deformation finite element method, the study gives numerical investigations of retrogressive slope failure in the 1994 Sainte-Monique slide, Quebec, with the focus on post-failure kinematics and retrogression patterns. The complete translational landslide evolution, with considerations of different 3D slope geometries, can be efficiently simulated using the depth-integrated finite volume method, capturing diverse post-failure behaviours, such as retrogression and blocky slide mass.

Keywords: Slope Stability, Sensitive Clays, Large Deformation Numerical Modelling, Retrogressive Failure

1. Introduction

Many natural clays undergo strain softening during shearing termed as sensitive clays. Offshore clay sediments are typical sensitive clays due to the bonded particle structure by surface charge under salty conditions, with soil sensitivity (ratio of peak and residual strengths) reported to be usually 2-6 (Randolph and Gourvenec 2011). Nearshore clay deposits originated from marine environment can have higher values of soil sensitivity as inter-particle salts disappear. In northern countries, such as Norway and Canada, sensitivity of the so-called 'quick clays' can be as high as over 100 (Crawford 1968). For slope failure in sensitive soils, shearing failure within a basal slip surface might lead to the growth of the slip surface, eventually evolving into a translational landslide such as the well-known enormous Storegga Slide offshore Norway (Kvalstad et al. 2005) or the massive retrogressive landslide in December 2020 at Gjerdrum, Norway, which caused seven deaths. A particular form of failure, which has been received considerable attention recently, is a retrogressive spreading failure with an uphill shear band propagation due to removal of downslope support (Locat et al. 2011, Zhang et al. 2019, 2021). Such phenomena occur in nature and are attributable to, for example, the erosion of riverbank and steep cut.

Because of greater computational capacity, studies have been able to consider 3D slope stability analysis in the last several decades (Hungr et al. 1989, Cheng and Yip 2007), although most of them have focused on rotational slide mechanisms using the Limit Equilibrium Methods. Some more sophisticated numerical models for slope stability problems have been emerging that use numerical methods such as the Finite Element Method (Griffiths and Marquez 2007). Another important issue in assessing the risk of slope instability is the modelling of landslide dynamics and its evolution, which can be performed by using large deformation numerical methods such as the depth-integrated method (Zhang and Puzrin 2021), computational fluid dynamics (Biscarini 2010), smoothed particle hydrodynamics (Zhang and Randolph 2020) and the material point method (Dong et al. 2017). However, most of these are 2D in nature and need the input of details of the initial slide mass such as geometry, volume and initial velocity, which are rarely determined in practice.

In this study, the whole evolution of translational landslides in sensitive soils, covering the failure initiation, slip surface growth, slab failure and post-failure behaviours, is observed and discussed through two numerical modelling methods: a 2D arbitrary Lagrangian-Eulerian method and a 3D depth integrated finite volume method.

The performance of the two numerical scheme in modelling translational landslides is compared and discussed in terms of three case studies.

2. Methodology

2.1 RITSS approach

The dynamic LDFE analyses of retrogressive failure during the 1994 SM slide were carried out using an approach termed remeshing and interpolation technique with small strain (RITSS, Hu and Randolph 1998; Zhang et al. 2015). Here a brief description of the numerical process is provided.

The RITSS approach falls in the category of the 'arbitrary Lagrangian-Eulerian' method. It divides a whole large-deformation analysis into a series of small deformation analysis increments, followed by remeshing and interpolation of all field quantities from old to new meshes. Four main modules: pre-processing, updated Lagrangian calculation, post-processing and interpolation, are necessary to fulfil each increment. One advantage of the RITSS method is that it can be implemented easily into combined commercial/non-commercial packages with each responsible for specific modules, though it was originated from an in-house Fortran package. Pre-processing, such as inputting parameters and meshing deformed slides, and updated Lagrangian calculations were undertaken by the commercial package Abaqus with minimal automation code. Interpolation of field quantities from old to new meshes were performed using a built-in algorithm in the commercial package Matlab. Post-processing, such as extractions of field quantities, nodal coordinates and model boundaries from old meshes, were fulfilled with Python codes. In each increment, finite strain theory was used and the equivalent plastic shear strain of less than unity was ensured to maintain the accuracy.

2.2 Depth-integrated finite volume method

The domain of interest is essentially divided into regularised cells, with each cell holding characteristics of the evolving landslide, as shown in Figure 1. The edges of the cell are parallel to the axes of coordinates *x* and *y*, and the *x*–*y* plane (*z* = 0) was set as the horizontal plane and crossing through a reference point (taken as the slope centre in the study) at the basal slip surface. Cells are fixed during the landslide process, with materials travelling through them, forming an Eulerian framework. Conservations of mass and momentum are then formulated within each cell, and global instability can be modelled by integrating all cells with consideration of proper inter-cell constitutive models and fluxes.

Conservation of mass in each cell can be expressed by

$$\frac{\partial h}{\partial t}+\frac{\partial hu}{\partial x}+\frac{\partial hv}{\partial y}=0 \tag{1}$$

where h is the height of the cell, u and v are the velocity in the x- and y-directions, respectively, and t is the elapsed time. Conservation of momentum in each cell is given by

$$\frac{\partial hu}{\partial t}+\frac{\partial hu^2}{\partial x}+\frac{\partial h\sigma_x}{\rho\partial x}+\frac{\partial huv}{\partial y}-\frac{\partial h\tau_{xy}}{\rho\partial y}-\frac{\tau_{w,x}+\tau_{g,x}}{\rho}=0 \tag{2}$$

and

$$\frac{\partial hv}{\partial t}+\frac{\partial hv^2}{\partial y}+\frac{\partial h\sigma_y}{\rho\partial y}+\frac{\partial huv}{\partial x}-\frac{\partial h\tau_{xy}}{\rho\partial x}-\frac{\tau_{w,y}+\tau_{g,y}}{\rho}=0 \tag{3}$$

for the x- and y-directions, respectively. In the above equations, σ_x, σ_y and τ_{xy} are stress components applied at the centre of the cell face, with the face normal parallel to the x or y axis; $\tau_{\mathrm{w},x}$ and $\tau_{\mathrm{w},y}$ are weak layer (or slip surface) shear stress components; and $\tau_{\mathrm{g},x}$ and $\tau_{\mathrm{g},y}$ are gravity shear stress components at the buried depth of the weak layer.

Two layers of fixed meshes with the same mesh size and alignment were taken, with the top layer used for solving mass and momentum conservation equations and the bottom layer tracking the changes in soil properties in the weak layer during slip surface growth. A finite volume method with staggered grids was used to integrate and solve the governing equations (1) to (3). Changes in soil properties during the landslide process are treated differently in the two layers. The soil properties, such as stress and strength, in the weak layer are

updated in the fixed mesh scheme based on the current values of h, u and v, assuming that the weak layer does not move with the sliding layer. As the sliding layer moves during the landslide process, its soil properties are updated at the deformed cell centre (based on current values of u and v) and interpolated to the original fixed centre after each time increment, in the spirit of the Arbitrary Lagrangian-Eulerian method.

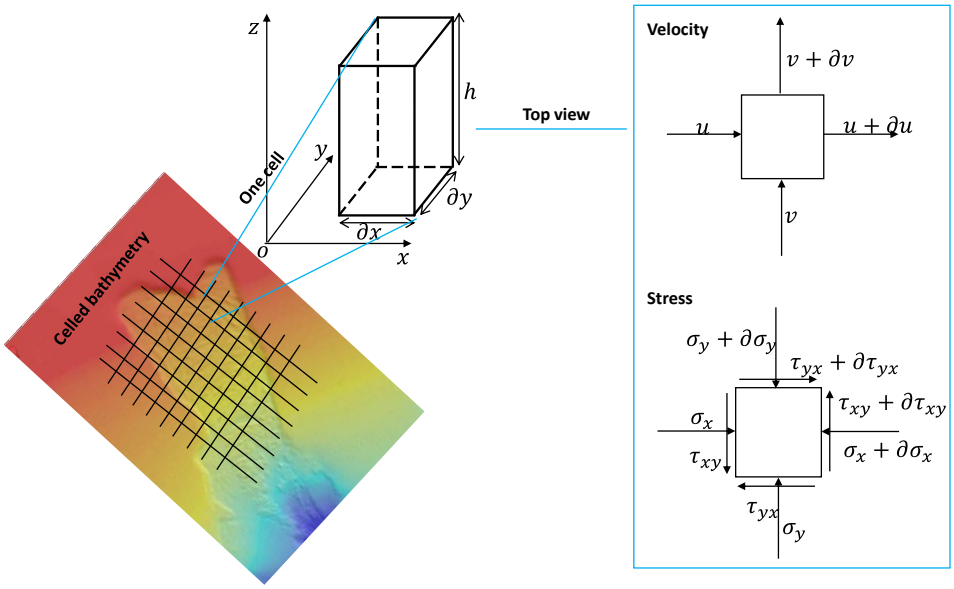

Figure 1: Discretisation of depth-integrated finite volume scheme (bathymetry image after Micallef 2013).

2.3 Strain softening of soils

A simple linear degradation relationship is given in Figure 2, which is sufficient to investigate post-failure retrogression behaviours though in most cases a non-linear strength degradation might be more relevant. It is assumed to comprise linear elastic response to peak shear strength, τ_p, followed by linear post-peak softening towards residual, τ_r. The plastic shear displacement to soften the shear strength to the residual is symbolised as δ_r^p. To implement the shear stress – shear displacement relationship into a solid element within the RITSS modelling, the relative shear displacement, δ, was related to the shear strain, γ, by

$$\delta = \gamma s \tag{4}$$

where s is the shear band thickness. Here, the element size through the model is roughly uniform with $s \approx 0.2$ m. In the elastic regime, the mobilised shear stress is calculated by

$$\tau = \bar{G}\delta^e = G_s\gamma^e \tag{5}$$

where G_s is the shear modulus with $\bar{G} = G_s/s$, γ^e is the elastic shear strain and $\delta^e = \gamma^e s$ represents the elastic shear displacement; in the plastic regime, the shear stress is limited to the softening shear strength which is governed by

$$\tau = max\left[\tau_p + (\tau_r - \tau_p)\frac{\delta^p}{\delta_r^p}, \tau_r\right] = max\left[\tau_p + (\tau_r - \tau_p)\frac{\gamma^p}{\gamma_r^p}, \tau_r\right] \tag{6}$$

where γ^p is the accumulated plastic shear strain with $\delta^p = \gamma^p s$ being the plastic shear displacement across the weak layer.

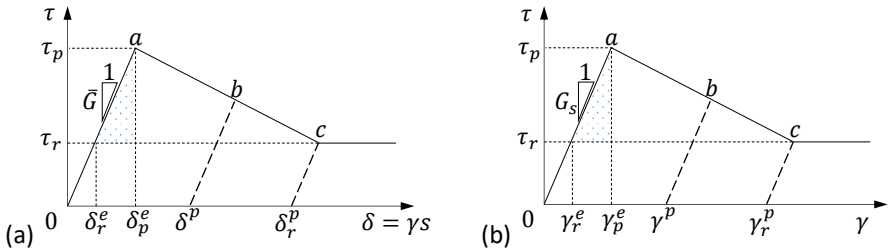

Figure 2: a) shear stress – shear displacement; and b) shear stress – shear strain relationship of strain softening soils (linear models are assumed).

3. Results and discussions

3.1 A comparison between the two methods

A series of 2D landslides were simulated using the two numerical schemes. For the depth-integrated FV method, the governing equations are tailored to fit for the 2D problems by ignoring the momentum in the *y*-direction (assuming the slide mass travels in the *x*-direction). A curvilinear slope model composed of an overlying layer and a weak layer was used. The weak layer is parallel to the slope surface and antisymmetric about the slope centre, which is set as the origin of the coordinate system. The weak layer geometry is described by

$$z = \begin{cases} -H\left[1 - exp\left(\frac{y}{H} tan\,\theta_c\right)\right], & y < 0 \\ H\left[1 - exp\left(-\frac{y}{H} tan\,\theta_c\right)\right], & y \geq 0 \end{cases} \tag{7}$$

where θ_c is the maximum slope angle at the centre, and H is the half-height of the slope. The peak undrained shear strength of the weak layer soil is fixed at $s_{\mathrm{uw,p}} = 10$ kPa. The undrained shear strength of the sliding layer, however, varies between $s_{\mathrm{us,p}} = 10$, 20, and 30, to simulate different post-failure behaviours. Other parameters are listed in Table 1. For the three cases with $s_{\mathrm{us,p}} = 10,\ 20$ and 30 kPa, active and passive failure are apparent at the upslope and downslope portion of the slope, respectively, as shown in Figure 3. With $s_{\mathrm{us,p}} = 10$ kPa, the upper layer soils are soft and flow downward after the global slab failure, with the layer becoming thinner upslope and thicker downslope. The relative strong sliding layer with $s_{\mathrm{us,p}} = 20$ and 30 kPa leads to break-up of the layer and a main scarp somewhere upslope. The two numerical schemes generate similar results in terms of the post-failure surfaces and failure patterns, which validates the methods with each other.

Table 1: Parameters for benchmark case.

Parameter	Value	Unit
Maximum slope angle, θ_c	6	degrees
Half slope height, H	20	m
Shear modulus, G	662.25	kPa
Shear stiffness in the weak layer, $\overline{\mathrm{G}}$	1656	kPa/m
At-rest earth pressure coefficient, K_0	0.75	
Gravity acceleration, g	9.81	m/s^2
Saturated density, ρ	1870	kg/m^3
Soil sensitivity in weak layer	5	
Residual plastic shear displacement, δ_r^p	0.2	m

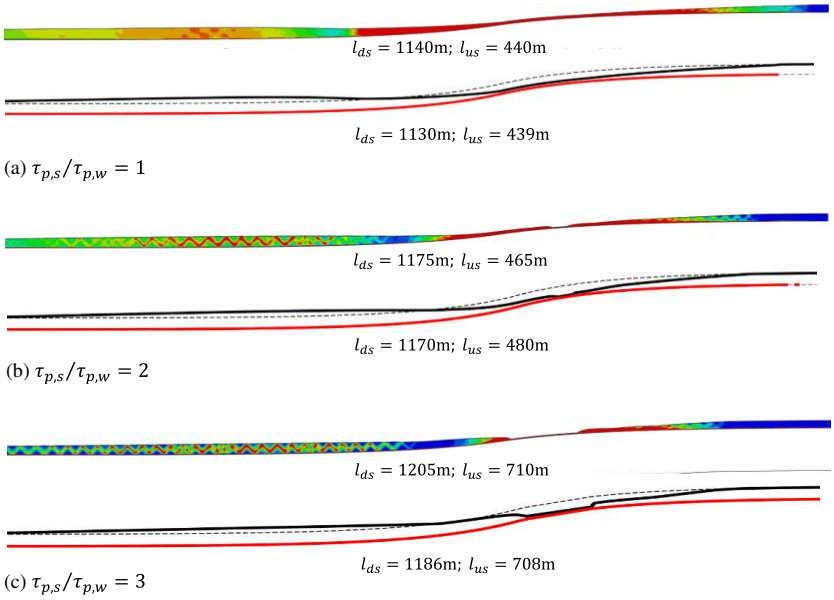

Figure 3: A comparison of the two numerical schemes.

3.2 Modelling the 1994 Sainte-Monique Slide with RITSS

On 21st April 1994, a retrogressive slide occurred along a brook in the municipality of Sainte-Monique (SM), Quebec, and simulated using the RITSS approach with details provided in Zhang et al. (2020). Geological and geotechnical investigations for determining the soil profile and properties, were carried out by the Ministry of Transport of Quebec in 2003 and 2004 (Locat et al. 2015). As shown in Figure 4, the sliding mass was restricted by the right-hand riverbank, with the brook fully filled by the sliding mass deposit. The retrogression distance by the 1994 event is about 105 m from the crest of the original slope to the backscarp of the slide, and the surface elevation after the event is at 32 m in general. Soil properties and other parameters were determined based on the documented geological and geotechnical investigations, as listed in Table 2.

Table 2: Soil properties and other parameters used to model the 1994 Sainte-Monique Slide.

Parameter	**Value**	**Unit**
Peak shear strength in sliding mass	33	kPa
Peak shear strength at shear surface	40	kPa
Soil sensitivity	10	
Plastic shear displacement to residual strength	0.1	m
At rest lateral earth pressure coefficient	0.5	
Soil unit weight	16	kN/m^3
Height of embankment	16.6	m
Slope angle of embankment	24	Degree
Width of riverbed	30	m

Figure 4 shows the contours of the current shear strengths during the slide process for the base case with properties shown in **Error! Reference source not found.**. The shear band initiates within the underlying shear s urface near the toe of the slope where the shear stress exceeds the peak undrained shear strength at $t = 0.5$ s. Unloading due to shear strength reduction during shearing leads to the shear band propagate to adjacent intact soils. First global failure is formed when the shear band develops from the shear surface to the crest of the embankment. After the global failure initiation at $t = 3.5$ s, the intact sliding mass breaks soon into several blocks and runs out along the riverbed. Retrogressive failure from the main backscarp is recognised and attributed to removal of support by run-out of the front sliding mass. The sliding blocks were torn apart into more pieces and gradually separate from each other at $t = 5.0$ s. Retrogression forms a complete failure surface through the riverbank leading to the second failure. The right-hand embankment acts as a barrier, arresting the

sliding mass from $t = 8.5$ s. The front block slows down during climbing the right-hand riverbank slope and is finally at rest at $t = 14.5$ s. Nearly half of the sliding mass deposits are fully softened at $t = 22.5$ s. Meanwhile, retrogressive failure is still active in the left-hand embankment continuing escalating the scale of the slide. The battle between retrogression and arrest of sliding mass ends at $t = 42$ s, when a stable configuration is formed. It is interesting to note that horsts and grabens are significant after fresh retrogressive failure but smashed into small blocks and even debris of the residual strength after dynamic run-out and 'rear-end' collisions near the right-hand embankment.

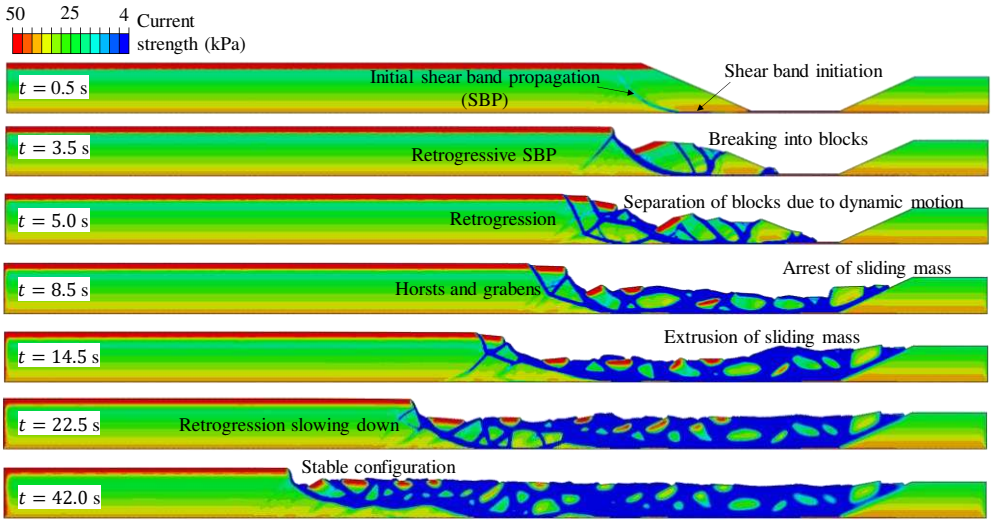

Figure 4: Contours of current shear strengths at different time during the 1994 SM slide.

3.3 Modelling 3D translational landslides with depth-integrated finite volume method

3D translational landslides with different slope geometries were simulated using the depth-integrated FM method in Zhang and Puzrin (2022), and an overview of the numerical results is given here. For the S-shape slope, the half-height of the slope in equation (7) was set to be the same with the planar slope, i.e., $H = 21$ m, and the maximum slope angle was taken as $\theta_c = 9°$ such that the average slope angle within the range of $-500\ \mathrm{m} < y < 500$ m approximates to the planar slope angle, i.e., 6°. The slope angle of the convex and concave slope models is the same with the planar slope model.

Figure 5 compares the final states of the four slope models with respect to the fields of the shear strength in the weak layer, the shear stress in the weak layer, the plastic strain in the sliding layer, and the normalised sliding layer thickness. It can be noted that the unaffected gravity shear stress fields from the four slope models are distinct. Some similarities can be identified in spite of different models: 1) retrogression appears upslope leaving a straight main scarp; 2) ploughing greatly extends the initial slab failure downslope forming a fan heave zone; 3) the heads of the mass transport deposits reach at about $y = -400$ m. Particularly, there are only slight differences between the results of the planar, convex and concave slopes, with slightly more horizontal slip surface growth pertained in the convex slope and slightly more retrogressive extension pertained in the concave slope. This reveals that the difference in the horizontal slope gradient among selected slope models has limited influence on the landslide evolution. In contrast, the final slip surface and mass transport deposit pertained in the S-shape curvilinear slope are significantly different from the other three models with less extended retrogressive failure and a smaller fan heave zone. This implies the slope gradient along the *y*-direction has a considerable effect on the landslide evolution.

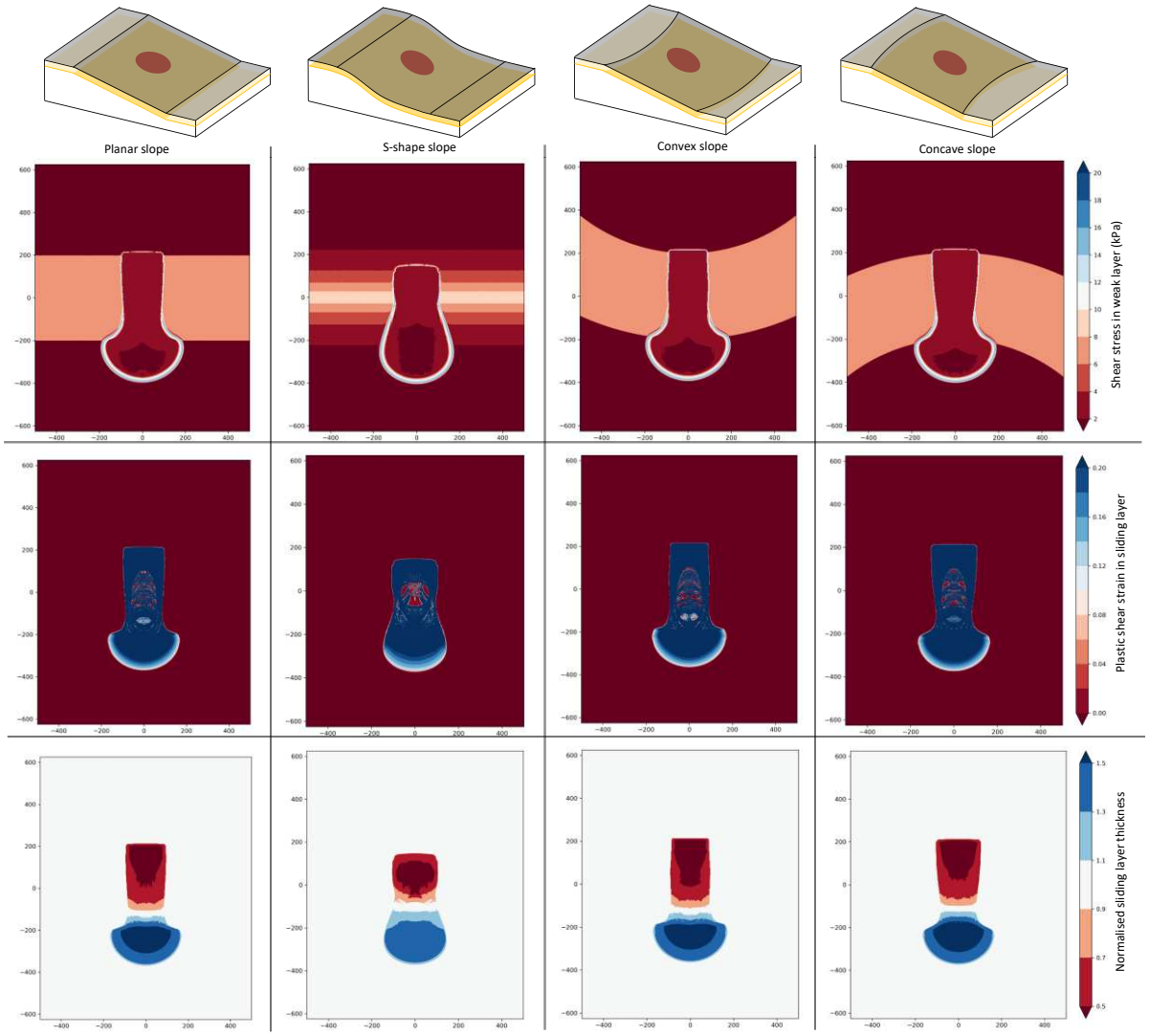

Figure 5: Morphology of the mass transport deposit in 3D translational landslides.

4. Conclusions

The study has proposed two numerical methods, including a remeshing and interpolation technique with small strain (RITSS) and a depth-integrated finite volume method, that can simulate the whole evolution of translational landslides in sensitive clays, including the failure initiation, shear band propagation, slab failure and post-failure dynamics. Diverse post-failure mechanisms, such as retrogression upslope and ploughing and run-out downslope, can be recorded through the proposed numerical schemes. The two numerical methods have been compared with a series of 2D translational landslides in terms of the post-failure surface and failure patterns. The 1994 Sainte-Monique slide in Quebec has been simulated by using the RITSS approach with focus on the evolution of the failure featured with the formation of horsts and grabens, that could not be observed through the depth-integrated FV approach. The depth-integrated FV approach, however, is more powerful in modelling large scale 3D translational landslides as demonstrated through modelling submarine landslides with various 3D slope geometries.

Acknowledgements

The author would like to thank Prof. Alexander Puzrin of ETH Zurich and Honorary Prof. Mark Randolph of the University of Western Australia for valuable discussions and guidance on the research topic.

References

Biscarini, C. (2010). Computational fluid dynamics modelling of landslide generated water waves. *Landslides*, 7: 117–124.

Cheng, Y. M. and Yip, C. J. (2007). Three-dimensional asymmetrical slope stability analysis extension of Bishop's, Janbu's, and Morgenstern–Price's Techniques. *J. Geotech. Geoenvironmental Eng.*, 133(12): 1544–1555.

Crawford, C.B. (1968). Quick clays of eastern Canada. *Engineering Geology*, 2 (4): 239-265.

Dong, Y., Wang, D. and Randolph, M. F. (2017). Runout of submarine landslide simulated with material point method. *Procedia Engineering*, 175: 357–364.

Griffiths, D. V. and Marquez, R. M. (2007). Three-dimensional slope stability analysis by elasto-plastic finite elements. *Géotechnique*, 57(6): 537–546.

Hu, Y., Randolph, M.F. (1998). A practical numerical approach for large deformation problem in soil. *Int J Numer Anal Methods Geomech*, 22 (5): 327–350

Hungr, O., Salgado, F. and Byrne, P. (1989). Evaluation of a three-dimensional method of slope stability analysis. *Canadian Geotechnical Journal*, 26(4): 679–686.

Kvalstad, T. J., Andresen, L., Forsberg, C. F., Berg, K., Bryn, P., Wangen, M. (2005). The Storegga slide: evaluation of triggering sources and slide mechanics. *Marine and Petroleum Geology*, 22(1-2): 245–256.

Locat, A., Leroueil, S., Bernander, S., Demers, D., Jostad, H.P, Ouehb, L. (2011). Progressive failure in eastern Canadian and Scandinavian sensitive clays. *Can. Geotech. J.*, 48(11): 1696–1712.

Locat, A., Leroueil, S. Fortin, A., Demers, D. Jostad, H.P. (2015). The 1994 landslide at Sainte-Monique, Quebec: geotechnical investigation and application of progressive failure analysis. *Can. Geotech. J.*, 52 (4): 490-504

Randolph, M.F. and Gourvenec, S. (2011). Offshore geotechnical engineering. Spon press, New York, USA.

Zhang, W. and Puzrin, A. M. (2021). Depth integrated modelling of submarine landslide evolution. *Landslides*, 18: 3063–3084.

Zhang, W. and Puzrin, A.M. (2022). How small slip surfaces evolve into large submarine landslides—Insight from 3D numerical modeling. *Journal of Geophysical Research: Earth Surface*, 127(7): e2022JF006640.

Zhang, W., Wang, D., Randolph, M. F. and Puzrin, A. M. (2015). Catastrophic failure in planar landslides with a fully softened weak zone. *Géotechnique*, 65(9): 755–769.

Zhang, W. and Randolph, M.F. (2020). A smoothed particle hydrodynamics modelling of soil–water mixing and resulting changes in average strength. *Int J Numer Anal Methods Geomech* ., 44(11): pp.1548-1569.

Zhang, W., Randolph, M. F., Puzrin, A. M. and Wang, D. (2019). Transition from shear band propagation to global slab failure in submarine landslides. *Can. Geotech. J.*, 56(4): 554–569.